IPNO DR 99–01

PROTON SCATTERING BY SHORT LIVED SULFUR ISOTOPES

F. Maréchal[1], T. Suomijärvi[1], Y. Blumenfeld[1], A. Azhari[2,3], E. Bauge[4], D. Bazin[2], J.A. Brown[2], P.D. Cottle[5], J.P. Delaroche[4], M. Fauerbach[2,3], M. Girod[4], T. Glasmacher[2,3], S.E. Hirzebruch[1], J.K. Jewell[5], J.H. Kelley[1], K.W. Kemper[5], P.F. Mantica[2,6], D.J. Morrissey[2,6], L.A. Riley[5], J.A. Scarpaci[1], H. Sheit[2,3], and M. Steiner[2].

[1] *Institut de Physique Nucléaire, IN_2P_3-CNRS, 91406 Orsay, France*
[2] *NSCL, MSU, East Lansing, Mi 48824, USA*
[3] *Department of Physics and Astronomy, MSU, East Lansing, Mi 48824, USA*
[4] *CEA, SPhN, BP 12, 91680 Bruyères-le-Châtel, France*
[5] *Department of Physics, FSU, Tallahassee, FL 32306, USA*
[6] *Department of Chemistry, MSU, East Lansing, Mi 48824, USA*

Proton Scattering by Short Lived Sulfur Isotopes

F. Maréchal[1,*], T. Suomijärvi[1], Y. Blumenfeld[1], A. Azhari[2,3,†], E. Bauge[4], D. Bazin[2], J.A. Brown[2,‡], P.D. Cottle[5], J.P. Delaroche[4], M. Fauerbach[2,3,*], M. Girod[4], T. Glasmacher[2,3], S.E. Hirzebruch[1], J.K. Jewell[5,§], J.H. Kelley[1,¶], K.W. Kemper[5], P.F. Mantica[2,6], D.J. Morrissey[2,6], L.A. Riley[5,♯], J.A. Scarpaci[1], H. Scheit[2,3,♭], and M. Steiner[2]

[1] *Institut de Physique Nucléaire, IN_2P_3-CNRS, 91406 Orsay, France*

[2] *National Superconducting Cyclotron Laboratory, Michigan State University, East Lansing, MI 48824*

[3] *Department of Physics and Astronomy, Michigan State University, East Lansing, MI 48824*

[4] *Commissariat à l'Energie Atomique, Service de Physique Nucléaire, Boîte Postale 12, 91680 Bruyères-le-Châtel, France*

[5] *Department of Physics, Florida State University, Tallahassee, FL 32306*

[6] *Department of Chemistry, Michigan State University, East Lansing, MI 48824*

(February 26, 1999)

Abstract

Elastic and inelastic proton scattering has been measured in inverse kinematics on the unstable nucleus ^{40}S. A phenomenological DWBA analysis yields a quadrupole deformation parameter $\beta_2 = 0.35 \pm 0.05$ for the 2_1^+ state. Consistent phenomenological and microscopic proton scattering analyses have been applied to all even-even Sulfur isotopes from $A = 32$ to $A = 40$. The microscopic analysis used microscopic collective model densities and a modified Jeukenne-Lejeune-Mahaux effective interaction. This analysis suggests the presence of a neutron skin in the heavy sulfur isotopes. The analysis is consistent with normalization values for λ_v and λ_w of 0.95 for both the real and

imaginary parts of the JLM potential.

PACS numbers: 21.10.Re, 25.40.cm, 25.40.Ep, 25.60.Bx

I. INTRODUCTION

Proton scattering continues to provide a wealth of information on nuclear structure and interaction potentials which are fundamental to nuclear physics. Such reactions have been extensively performed with stable nuclei and form an important part of the foundation of our current understanding of nuclear systems. However, the valley of β-stability is only a very limited area of the nuclear chart and several theoretical calculations predict drastic modifications in the structure of nuclei outside the valley of stability. In particular, great current interest is focused on neutron rich nuclei near the $N = 28$ magic number for which shell closure is expected to vanish, yielding a new deformation region [1–3]. Excitation energies and B(E2) values of the first 2^+ states in neutron rich sulfur and argon isotopes have been previously measured by intermediate energy Coulomb excitation [4,5]. The present proton scattering results are complimentary to those obtained by Coulomb excitation because the electromagnetic excitation mainly probes the protons in the nucleus, while proton scattering at energies around 30 MeV, is mainly sensitive to the neutrons. By combining the two measurements, it should be possible to probe the neutron and proton densities and deformations. Such studies are particularly appealing for nuclei far from stability, where isospin effects are expected to be important.

The Coulomb force is known exactly, so analyses of Coulomb excitation experiments are model independent. On the other hand, extracting nuclear properties from proton scattering relies on interaction models, the parameters of which must be adjusted to reproduce experimental results. Generally, proton scattering data are analyzed by using phenomenological optical potentials and standard collective form factors. Summaries of many studies on stable nuclei have yielded optical model parametrizations such as that by Becchetti and Greenlees [6], which give good predictions for scattering cross sections. However, such approaches may encounter difficulties far from stability due to the assumption of similar interaction potentials for neutrons and protons. Moreover, the extracted parameters do not give direct access to the nuclear densities. An alternative method is to use a microscopic approach where

nuclear densities are folded with an effective nucleon-nucleon interaction to produce the optical model potential. Once the parameters of the effective interaction are fixed, this analysis should be sensitive to unusual nuclear density distributions such as neutron halos or skins. This approach with nuclei far from stability should also lead to a refined determination of the effective interaction and in particular its isospin dependence.

The recent availability of radioactive beams with substantial intensities and reasonable optical qualities, has allowed measurements of proton scattering on short lived nuclei in inverse kinematics, using proton targets. Two-body reaction kinematics can be determined either by detecting the outgoing heavy nucleus or by measuring the energy and angle of the recoiling light particle. At present, such studies are restricted to nuclei that lie closer to stability than for half-life or Coulomb excitation measurements, since the prerequisite of very thin targets, which preserve the kinematic characteristics of the recoiling protons, requires beam intensities of at least several 10^3 particles per second. Therefore, proton inelastic scattering data with unstable beams are still scarce [7–9].

We have undertaken a study of neutron rich sulfur isotopes through proton scattering in inverse kinematics. The first experiment was performed using a secondary fragmentation beam of ^{38}S delivered by the National Superconducting Cyclotron Laboratory at Michigan State University (NSCL/MSU). Excitation energy spectra and angular distributions were obtained through the measurement of the energies and angles of recoiling protons with a silicon-strip detector array. A large deformation parameter $\beta_2 = 0.35 \pm 0.04$ was extracted for the first 2^+ state in ^{38}S from calculations using standard Wood-Saxon phenomenological optical potentials. Comparison with the results of the Coulomb excitation experiment [4] indicated an isovector contribution to the 2_1^+ state of ^{38}S. These results have already been published in Refs. [10,11].

Here, we present the results of elastic and inelastic proton scattering experiment on the unstable nucleus ^{40}S performed at the NSCL/MSU with an experimental setup similar to that used in the ^{38}S experiment. The data were collected over a broad angular range and the value of β_2 was extracted for the 2_1^+ state in ^{40}S. In addition to the standard phenomenological

analysis, a complete microscopic analysis using microscopic collective model densities folded with a modified Jeukenne-Lejeune-Mahaux (JLM) effective interaction is presented. The availability of proton scattering data for the stable nuclei ^{32}S [12], ^{34}S [13] and ^{36}S [14] allowed us to apply this analysis to a long isotopic chain crossing the major $N = 20$ shell closure.

The paper is organized as following. The second section is devoted to the experimental procedure used for the ^{40}S experiment and the third to the extraction of the experimental angular distributions. The fourth section presents the phenomenological analysis and compares the deformation parameters obtained for different even-even sulfur isotopes. The microscopic analysis is presented in the fifth section and the presence of a possible neutron skin in the unstable neutron rich isotopes is discussed. Our findings are summarized and conclusions are drawn in section six.

II. EXPERIMENTAL PROCEDURE

A. Beam Parameters

The secondary ^{40}S beam was produced by fragmentation of a primary 60 MeV/nucleon ^{48}Ca beam, provided by the K1200 cyclotron at the National Superconducting Cyclotron Laboratory, on a 285 mg/cm^2 Be target. The fragments were analyzed using the A1200 fragment separator [15], and the resulting beam was purified by using a 70 mg/cm^2 aluminum wedge placed in the second dispersive image point of the A1200. The ^{40}S beam had a final intensity of 2000 particles per second and an energy of 30 MeV/nucleon.

The maximum 3% momentum acceptance of the A1200 fragment separator was used, yielding a large energy spread ΔE/E=6% and a beam purity not higher than 15%, the beam being mainly contaminated by ^{43}Ar. The beam particles were identified event by event by a time-of-flight measurement combined with a total energy measurement. The energy was measured by a ΔE-E phoswich detector consisting of thin and thick fast plastic scintillators

placed at 0° and a distance of 40.6 cm behind the secondary target covering angles up to Θ_{lab}=5.4° (see Fig. 1). The time-of-flight was measured between the 0° detector and a plastic scintillator placed at the exit of the A1200 separator over a flight path of 36 m. This allowed the data for ^{40}S and ^{43}Ar to be separated off-line. Results on ^{43}Ar scattering will be presented in a forthcoming paper [16]. Moreover, the time-of-flight measurement allowed the energy of the secondary beam to be determined on an event-by-event basis with a resolution of about 1%. Due to the large emittance of the secondary ^{40}S beam, $\sim 100\pi$ mm-mrad, two Parallel Plate Avalanche Counters (PPAC) [17], placed 82 cm and 183 cm upstream from the target, were used to measure event by event the incident beam angle and beam position on the target. The position resolution given by the PPACs was about 2 mm, corresponding to a resolution of about 0.18^o for the incident angle on target.

It is important to note that the experimental conditions are much more challenging than those encountered in the case of the former ^{38}S experiment [10]. In the former case a primary ^{40}Ar beam yielded an ^{38}S rate of 2×10^5 pps. The beam was then collimated sufficiently so that it was unnecessary to carry out event-by-event ray tracing, retaining an intensity of 3×10^4 pps, an order of magnitude larger than in the present case of ^{40}S. Moreover, the energy of the 2_1^+ state of ^{38}S (1.29 MeV) is higher than that of ^{40}S (0.89 MeV), making its kinematical separation from elastic scattering easier.

B. Setup for the measurement of recoiling protons

The sulfur projectiles were scattered by a very thin 2 mg/cm^2 $(CH_2)_n$ target rotated to an angle of about 30° with respect to the beam direction, thus providing an effective in beam target thickness of 2.3 mg/cm^2, while limiting the energy loss and angular straggling of low energy recoiling protons. An array of 8 telescopes, 5×5 cm^2 active area each, was used to measure the energies and the angles of the recoiling protons. The telescopes, four on either side of the beam, were positioned 29 cm from the target and covered laboratory angles between 56° and 89°. A schematic diagram of the experimental setup is shown in

Fig. 1. Figure 2 shows the calculated energy-angle correlation for the kinematics of recoiling protons. The angular range covered by each telescope is indicated by the areas between the vertical lines in Fig. 2.

Each telescope was composed of a 300 μm thick silicon strip detector with 16 vertical strips (3 mm wide) backed by a 500 μm thick silicon detector and a 1 cm thick stopping cesium-iodide detector which was read out by 4 photodiodes. The silicon detectors were calibrated by using a ^{228}Th alpha source. The response of the CsI detectors strongly depends on the detected particle and therefore they were calibrated by using elastic scattering of protons on a gold target at various incident energies up to 22 MeV. The energy resolution obtained with the silicon detectors was about 50 keV compared to about 7% with the CsI. The 3 mm strip pitch corresponds to an angular resolution of 0.6°. It should be noted that the large uncertainty $\Delta\phi$ corresponding to the detector size in the absence of horizontal strips has only a minor influence on the resolution because the detectors are placed rather close to 90°.

For particles that stopped in the Si-strip detector, the proton identification was achieved by time-of-flight and energy measurements. The time-of-flight was measured between each individual strip and the 0° plastic detector. A relatively good timing resolution of about 1 ns for 3 MeV protons was obtained. For higher energy particles that punched through the first detector, the particle identification was obtained by a ΔE-E measurement in Si-Si or Si-CsI. The poor energy resolution of the CsI was sufficient to identify the particles but the residual energy was deduced from the energy losses in the two first silicon detectors. This setup allowed us to measure protons from about 1 MeV up to 50 MeV corresponding to an excitation energy range of about 5 MeV and a center-of-mass angular range between $\Theta_{cm} = 15°$ and $\Theta_{cm} = 45°$.

The proton events in the silicon strip telescopes were selected with the requirement that a heavy projectile must have survived the collision and have been detected in the 0° detector. Note that the opening angle of this detector was large enough to detect scattered projectiles with unit efficiency. The coincidence requirement between protons and ejectiles

very effectively reduced the background due to reactions with the carbon in the CH_2 target.

III. EXPERIMENTAL RESULTS

Figure 3(a) displays the data in an energy vs. angle scatterplot obtained for protons recoiling into the telescopes centered at 70° in coincidence with ^{40}S ejectiles. The scattering angle has been corrected for the incident beam angle as well as for the impact position on the target. The resolution for the recoil angle is estimated to be 0.95°, the main contribution coming from the width of the strips. The solid and dashed lines in Fig. 3(a) show the expected energy-angle correlation for the ground state (g.s.) and the 2_1^+ state, which was previously determined to have an excitation energy of 891 keV by Coulomb excitation [4]. Events corresponding to the 2_1^+ state are clearly observed, but this state cannot be separated from the elastic scattering line over the whole angular range. Some indication for a higher lying state is also present. It should be noted that the background is very low. For comparison, a similar plot obtained in the ^{38}S experiment [10] is displayed in Fig. 3(b). As mentioned before, the statistics are much higher and the 2_1^+ state is well separated from the elastic scattering over the entire measured angular range, emphasizing once again the very challenging nature of the present ^{40}S experiment.

The recoil data were transformed to the center-of-mass frame using relativistic kinematics. An event-by-event measurement of the projectile energy was carried out, thus taking into account the incident energy spread of 6%. The data were corrected for the geometrical acceptance of the telescopes and an absolute normalization was obtained by using the number of incident particles observed in the 0° detector and the target thickness.

Figure 4 displays the excitation energy spectrum for ^{40}S, integrated over the center-of-mass angular range $20° \leq \Theta_{cm} \leq 46°$ (a) and that restricted to the 28°-36° angular bin where the elastic scattering cross-section exhibits a minimum (b). We clearly identify the first 2^+ state located at 860 ± 90 keV in good agreement with the value obtained in the Coulomb excitation experiment, 891 ± 13 keV [4]. The excitation energy resolution, which

strongly depends on the recoil angle resolution, is about 750 keV for center of mass angles around 30°. This resolution, obtained with an unstable beam, is on the same order of magnitude as the resolution measured in a test experiment of the apparatus [10] which was proton scattering with a stable ^{40}Ar beam at 40 MeV/nucleon that had a small emittance and no beam tracking. This result shows that the incident trajectory reconstruction and the beam energy measurement, event by event, allows us to recover the intrinsic qualities of the detection system.

Figure 5 shows the angular distributions for the ground state and the first 2^+ excited state of ^{40}S. Since it is very difficult to separate the elastic scattering from the inelastic scattering over the whole angular range in the center-of-mass frame, we have first extracted the so-called quasi-elastic scattering angular distribution. This distribution, which corresponds to the sum of the elastic scattering and inelastic scattering to the state located at 860 keV, was obtained by projecting the contents of a contour surrounding both states, in the excitation energy vs. Θ_{cm} plane. The elastic cross-section, shown by the open circles on Fig. 5, was then obtained by subtracting the calculated inelastic cross-section (see section IV) from the experimental quasi-elastic cross-section. The two points for the inelastic angular distribution were obtained by fitting the elastic and inelastic peaks for two different angular bins (see Fig. 4) with two Gaussians and then integrating the number of counts. Unfortunately, the very low statistics do not allow us to clearly identify the inelastic contribution for other angles where the elastic scattering dominates the count rate. The center-of-mass angular resolution was estimated to be 1.93°. The error bars on Fig. 5 are purely statistical. In the case of elastic scattering a complete angular distribution between $\Theta_{cm} = 15°$ and $\Theta_{cm} = 45°$ was obtained and the first diffraction minimum was clearly mapped out.

IV. PHENOMENOLOGICAL ANALYSIS

A. The ^{40}S nucleus

Proton scattering data are generally analyzed with the Distorted Wave Born Approximation (DWBA) using phenomenological optical potentials to extract deformation parameters for the low-lying collective states. Here we have performed DWBA calculations with the code ECIS [18] using a standard vibrational form factor for the calculation of the inelastic cross-section. The optical potential parameters were taken from the Becchetti-Greenlees parametrization [6], which was developed for (p,p) scattering on $A \geq 40$ nuclei. The results of the calculations are shown by the solid lines in Fig. 5. In the case of elastic scattering, no arbitrary normalization of the data was required, the calculated cross section is directly compared to the absolute experimental cross section in Fig. 5. Excellent agreement is observed, indicating that the parametrization proposed by Becchetti and Greenlees for stable nuclei works well for elastic scattering of sulfur isotopes far from stability.

In order to extract the value of the β_2 deformation parameter, the inelastic scattering calculation was normalized to the 2_1^+ cross-section. This procedure yields a value of $\beta_2 = 0.35 \pm 0.05$ for the nucleus ^{40}S. The error corresponds to the minimum and maximum β_2 values for which the calculation still coincides with the data points within experimental error.

The combination of measurements of inelastic hadron scattering and electromagnetic excitation (such as Coulomb excitation) of the same nuclei are interesting since they can provide a way to disentangle proton and neutron contributions to the studied transition. In the case of inelastic proton scattering at a few tens of MeV incident energy, the neutron interaction strength is 3 times larger than the proton one [19]. Therefore, proton scattering mainly probes the distribution of neutrons in the nucleus. In contrast, Coulomb excitation measures the electromagnetic matrix element $B(E2; 0_{gs}^+ \rightarrow 2_1^+)$ which is directly related to the proton multipole transition matrix element M_p by $B(E\lambda, J_i \rightarrow J_f) = M_p^2/(2J_i + 1)$.

Thus, measurements of the deformation parameters with the two different probes allows us to determine the ratio between the neutron and proton multipole transition matrix elements M_n/M_p. In the phenomenological approach, this ratio is calculated using the formula derived in Ref. [20]

$$\frac{M_n}{M_p} = \frac{b_p}{b_n}\Big[\frac{\delta}{\delta_{em}}\Big(1 + \frac{b_n}{b_p}\frac{N}{Z}\Big) - 1\Big], \tag{1}$$

where b_p and b_n are the interaction strengths of incident protons with target protons and neutrons respectively, δ is the deformation length from (p,p') scattering and δ_{em} is the electromagnetic deformation length ($\delta = \beta_2 r_0 \mathrm{A}^{1/3}$). An r_0 value of 1.17 fm which corresponds to the radius parameter of the Becchetti-Greenlees systematics was used for (p,p') scattering, while $r_0 = 1.20$ fm was taken for electromagnetic excitation. The b_p and b_n values were taken as 0.3 and 0.7, respectively [21]. This yields $M_n/M_p = 1.88 \pm 0.38$ for the 2_1^+ state in ^{40}S, and thus $M_n/M_p = (1.25 \pm 0.25)N/Z$. An isoscalar excitation should have an M_n/M_p ratio equal to the neutron to proton ratio N/Z in the framework of the collective model, meaning that protons and neutrons participate equally in the excitation of the nucleus. The value obtained for ^{40}S therefore suggests a small isovector contribution to the 2_1^+ excitation.

B. The sulfur isotopic chain

An exciting aspect of radioactive beam studies is the search for the onset of major structural changes that may occur in nuclei far from stability. The sulfur isotopic chain presents an interesting opportunity for such a study since the 2_1^+ states of the even-even isotopes have been measured with both hadronic and electromagnetic probes.

Proton scattering data have been measured for the even-even stable isotopes ^{32}S at 29.6 MeV [12] , ^{34}S at 29.8 MeV [13] and ^{36}S at 28.0 MeV [14] as well as for the unstable nucleus ^{38}S at 39.0 MeV [10]. The elastic and inelastic angular distributions taken from these studies, as well as those from the present study of ^{40}S are displayed in Fig. 6. The reported $\beta_2^{pp'}$ values are presented in Table I. In order to check the consistency of the

values obtained with different prescriptions for the optical potential, we have reanalyzed the published data for the stable sulfur isotopes using the Becchetti-Greenlees optical potential, following the same procedure used for ^{40}S. The results are compared to the data in Fig. 6 and the $\beta_2^{pp'}$ values extracted from this analysis are given in Table I. A good description of the angular distributions over the whole isotopic chain was obtained and the deformation parameters agree within the error bars with the values extracted in the original analyses of Refs. [12–14], except for the case of ^{34}S where the present reanalysis gives a slightly lower value of $\beta_2 = 0.24 \pm 0.02$ compared to the original value of 0.28 ± 0.01 [13].

The B(E2) values and related electromagnetic β_2^{em} values for the 2_1^+ states, known from the systematics of adopted values [22] for the stable isotopes, and from recent Coulomb excitation measurements for ^{38}S and ^{40}S [4] are also given in Table I. The M_n/M_p values, listed in Table I, were calculated using Eq. (1) with the $\beta_2^{pp'}$ (BG) values taken from the present reanalysis using the Becchetti-Greenlees potential.

From a general standpoint, we first note the unusual behavior of ^{36}S, with a very high 2_1^+ excitation energy and very low $\beta_2^{pp'}$ and β_2^{em} values, that is similar to the behavior generally observed for doubly magic nuclei. Moving to ^{38}S and ^{40}S by adding neutrons to the $f_{7/2}$ shell one observes a sudden decrease of the 2_1^+ excitation energy and increase of both β_2 values. A similar, but less pronounced, trend is observed for ^{34}S and ^{32}S as neutrons are removed from the $N = 20$ closed shell. A remarkable feature is that the $\beta_2^{pp'}$ and β_2^{em} for ^{32,34}S are comparable whereas for the neutron-rich S isotopes $\beta_2^{pp'}$ is significantly larger than β_2^{em}. For these two heaviest nuclei, we expect the neutron excess to play a major role in the 2_1^+ state excitation. It is also interesting to note that very little change of the deformation parameters is discernible between ^{38}S and ^{40}S.

Significant evolution of the M_n/M_p values is also observed along the sulfur isotopic chain. As mentioned above, a value equal to N/Z corresponds to an isoscalar model in which protons and neutrons participate equally in the excitation of the nucleus. However, a marked departure from this behavior is observed for single closed shell nuclei. For instance, we expect mainly neutrons to participate in the excitation of a nucleus with a proton shell

closure, yielding an M_n/M_p ratio greater than N/Z. A typical example of such behavior is observed in the Sn isotopic chain [21] where isotopes between $A = 116$ and 124 exhibit an M_n/M_p ratio around $1.4 \times N/Z$. The M_n/M_p values extracted for ^{38}S and ^{40}S are similarly greater than N/Z and no significant change is observed between these two isotopes.

The phenomenological analysis of the proton scattering data indicates a sudden change in the collective properties of the sulfur isotopes when moving from ^{36}S (which resembles a doubly closed shell nucleus) to ^{38}S. Very little change in the extracted parameters is observed when adding two more neutrons forming ^{40}S. To investigate if the observed evolution can be related to properties of the matter and transition densities of nuclei under study, and in particular the eventual appearance of a neutron skin, a microscopic analysis of the data will be presented next.

V. MICROSCOPIC ANALYSIS

A. Description of calculations

In a microscopic approach to scattering processes, one can view the nucleon-nucleus optical model potential (OMP) as the result of the folding of a complex, energy and density dependent effective interaction with the nuclear density. In the present study, we will be extending the spherical OMP work published in Ref. [23] to treat proton scattering by deformed nuclei.

The (p,p') scattering analysis shown below uses deformed OMPs in which point proton and neutron radial densities are calculated through a microscopic collective model for quadrupole motion. This model has proved successful in analyses of charge and transition densities measured in electron scattering experiments [24]. Briefly, a collective Hamiltonian H_{coll} expressed in terms of the five quadrupole collective degrees of freedom is built from constrained Hartree-Fock-Bogoliubov calculations based on the finite range, density-dependent D1S force [25]. Solving H_{coll} provides energies (E_i) and wave functions ($|I_i>$) of ground

and excited states. Radial densities for protons and neutrons in a nucleus are then deduced from the matrix elements of the operators

$$\hat{\rho}_{p(n)}\ (\vec{r}) = \sum_{i=1}^{Z(N)} \delta(\vec{r} - \vec{r_i}), \tag{2}$$

where Z and N are the proton and neutron numbers, respectively. Only the $\lambda = 0$ and 2 multipoles of the density distributions are actually considered in the (p,p') analyses. Their components are written (with $\tau = p$ or n)

$$\rho_{\tau\ (\lambda=0)}(r)\ Y_{00}(\theta) =< 0^+_{gs}|\ \hat{\rho}_\tau\ (\vec{r})|0^+_{gs} >\ Y_{00}(\theta) \tag{3}$$

for the ground state, and

$$\rho_{\tau\ (\lambda=2)}^{0^+_{gs}\rightarrow 2^+_1}(\vec{r}) =< 2^+_1|\ \hat{\rho}_\tau\ (\vec{r})|0^+_{gs} >\ Y_{20}(\theta) \tag{4}$$

for the $0^+_{gs} \rightarrow 2^+_1$ transition and

$$\rho_{\tau\ (\lambda=2)}^{2^+_1\rightarrow 2^+_1}(\vec{r}) =< 2^+_1|\ \hat{\rho}_\tau\ (\vec{r})|2^+_1 >\ Y_{20}(\theta) \tag{5}$$

for the $2^+_1 \rightarrow 2^+_1$ reorientation transition. For more details, see Ref. [24]. In these calculations, no effective charges and free parameters are introduced.

The nuclear densities calculated as shown above were then folded with a nucleon-nucleon effective interaction $\mathcal{U}^{JLM}$ which we refer to as the JLM interaction. This interaction is a hybrid in which the energy- and density-dependent, spin-independent interaction in nuclear matter comes from the original work of Jeukenne, Lejeune, and Mahaux [26–29] with a new parameterization defined in Ref. [23]. As in Ref. [23], the imaginary part of the effective interaction was multiplied by an effective mass as pointed out in Ref. [30]. Although the JLM interaction has been established for nuclear matter, it can be applied to finite nucleus potentials by using the local density approximation (LDA) or the improved LDA as shown in Ref. [29]. This improved LDA is extended to deformed nuclei in Refs. [14,31]. The improved LDA for the diagonal potential is given by

$$U_{diag}(r, E) = (t\sqrt{\pi})^{-3} \int \rho(r')\ \mathcal{U}^{JLM}(\rho(r_i), E)\ \exp(-|\vec{r} - \vec{r'}|^2/t^2)\ d\vec{r'}, \tag{6}$$

while the $0^+_{gs} \rightarrow 2^+_1$ transition (or $2^+_1 \rightarrow 2^+_1$ reorientation) potential is

$$U_{tr}(r,E) = (t\sqrt{\pi})^{-3} \int \rho_{tr}(\vec{r'})\, \mathcal{U}^{JLM}_{tr}(\rho(r_i),E)\, \exp(-|\vec{r}-\vec{r'}|^2/t^2)\, d\vec{r'}. \quad (7)$$

Here $\mathcal{U}^{JLM}(\rho,E) = U^{JLM}(\rho,E)/\rho$, t is the range of the effective interaction, $\rho(r)$ is the matter radial density ($\rho = \rho_n + \rho_p$, see Eq. (3)), $\rho_{tr}(\vec{r})$ is the transition (or reorientation) density (see Eq. (4) or Eq. (5)) and r_i is the point where the effective interaction is evaluated. The transition interaction $\mathcal{U}^{JLM}_{tr}(\rho,E) = (1+\rho\,\partial/\partial\rho)\,\mathcal{U}^{JLM}(\rho,E)$ is enhanced by the additional density dependence defined in Ref. [32]. The position r_i at which the interaction is evaluated can be chosen according to several prescriptions [23,31] thus defining different improved LDAs. In this study, the effective interaction is taken to be the arithmetic mean of the interactions evaluated at the projectile position (r) and at the target position (r'). As suggested in Ref. [23], the range of the effective interaction has been taken to be equal to 1.2 fm. The Coulomb correction was included by evaluating the central interaction at $E - V_c(r)$ where $V_c(r)$ is the the Coulomb potential and E the incident energy. The complex central proton OMP (U) defined above is composed of an isoscalar (U_0) and an isovector (U_1) part; it is written $U = U_0 - \alpha\, U_1$, where $\alpha(\vec{r}) = (\rho_n - \rho_p)/(\rho_n + \rho_p)$ is the asymmetry parameter, and $\rho_n(\vec{r})$ and $\rho_p(\vec{r})$ are the point neutron and proton radial densities, respectively. Finally, in order to better account for experimental scattering measurements, we allow for small phenomenological normalizations of the real and imaginary potential depths, which are multiplied by λ_v and λ_w, respectively.

Since no spin-orbit interaction is provided by the nuclear matter based approach of JLM, we rely on the Scheerbaum prescription [33] extended to deformed nuclei, along with the energy dependent potential depths shown in Ref. [23] to calculate the deformed complex spin-orbit potential in the full Thomas form [34].

Once the diagonal and transition potentials have been obtained, they were inserted into the ECIS98 code [18] to solve the coupled equations for elastic and inelastic proton scattering by the 0^+ ground states and 2^+_1 excited states of the even-even sulfur isotopes. A reorientation $2^+_1 \rightarrow 2^+_1$ potential is included in the coupling scheme, and is calculated using Eq. (7)

along with the $2_1^+ \rightarrow 2_1^+$ transition density calculated above. Finally, Coulomb excitation is accounted for.

B. Results

The point neutron and proton ground state densities as well as the $0_{gs}^+ \rightarrow 2_1^+$ transition densities calculated with the microscopic collective model are displayed in Fig. 7. In the case of the $N = Z$ nucleus ^{32}S, the proton and neutron densities are very similar. For ^{34}S and ^{36}S, the calculation predicts that the differences due to the additional neutrons show up mainly in the interior of the nucleus, and both transition densities peak at the same radius. Moving to the more neutron rich isotopes ^{38}S and ^{40}S, a clear indication of a neutron skin is observed in the ground state densities. Moreover, for these two isotopes, the neutron transition densities are peaked at larger radii than for protons. The scattering process is mainly sensitive to the surface properties of the target nucleus at the proton energy of a few tens of MeV considered in this study.

Model-dependent quadrupole deformation parameters were calculated using

$$\beta_2^{n(p)} = \frac{\sqrt{5\pi}\, Q_2^{n(p)}}{3\, N(Z)\, R^2} \tag{8}$$

where $Q_2^{n(p)}$ is the neutron (proton) quadrupole moment, R is the nucleus radius defined as $r_0 A^{1/3}$ ($r_0 = 1.2$ fm) and $N(Z)$ is the neutron (proton) number. These deformation parameters for the neutron, proton and matter distributions are listed in Table II along with the calculated excitation energies of the 2_1^+ state and the rms charge radii. The quadrupole deformation calculated for ^{36}S is dramatically overestimated compared with those coming from the Coulomb excitation and proton scattering results shown in Table I. For the other sulfur isotopes, the predicted quadrupole deformations exhibit somewhat better agreement with the phenomenological ones. Yet, excluding ^{36}S, the calculated quadrupole deformations become smaller near the $N = 20$ closed shell. This behavior is comparable to that exhibited by the phenomenologically derived deformation parameters, and can be understood using

the same $N = 20$ shell closure arguments. The case of ^{36}S is not thoroughly understood, but collective models such as the one used in this study are known to be far from ideal when applied to nuclei whose potential wells are very steep, like in the case of closed shells, and particularly for $N = 20$. Note that in Table II, consistent with our discussion of Fig. 7, the neutron deformations for ^{38}S and ^{40}S are predicted to be slightly larger than the proton ones. Similarly, phenomenological analyses yield a higher deformation value for (p,p') scattering which is preferentially probing neutron densities than for Coulomb excitation, which is only sensitive to charge distributions.

Direct comparison between experimental and calculated charge densities for the ground state and the $0^+_{gs} \rightarrow 2^+_1$ transition are shown in Fig. 8 for ^{32}S, ^{34}S and ^{36}S. Comparison with the experimental ground state densities [35] shows that the microscopic calculations underpredict the density in the inside of the nucleus, and very slightly overpredict it at the surface, consistent with the 1.5 to 2.5% overestimation of the experimental charge rms radii (see Table I) by the collective Hamiltonian calculations (see Table II). Comparisons between calculated and measured charge transition densities for ^{32}S [36,37] and ^{34}S [38] show that the amplitudes of the calculated $0^+_{gs} \rightarrow 2^+_1$ transition densities are larger than the measured ones by about 10%. This difference is consistent with the slight overprediction of the quadrupole deformations exhibited by the ^{32}S and ^{34}S calculations. Nevertheless, for ^{32}S and ^{34}S, the overall shape and amplitude of the predicted charge and transition distributions closely match those of the experimental distributions. The neutron and proton transition matrix elements M_n and M_p can be calculated from the transition densities by

$$M^{\lambda}_{n(p)} = \int_0^{\infty} \rho^{n(p)}_{tr,\lambda}(r)\, r^{\lambda+2}\, dr, \tag{9}$$

where $\rho^{n(p)}_{tr,\lambda}$ is the neutron (proton) transition density to the excited state and λ is the transition multipolarity, in this case $\lambda = 2$. The M_n/M_p ratio values, listed in Table II, roughly follow the same trend as those extracted from the phenomenological analysis.

As described in the previous subsection, it is necessary to determine the renormalization parameters λ_v and λ_w of the strength of the optical model potential in order to calculate

angular distributions. Different studies of (p,n) charge exchange reactions have shown that the original isovector part of the JLM interaction is too weak by almost a factor of 2 [39,40]. This weakness was usually compensated by ad-hoc normalizations of both the isoscalar and isovector terms of the potential. However, in our case this procedure leads to smaller λ values for ^{32}S than for the other sulfur isotopes. On the other hand, an excellent representation of the elastic scattering data over the entire sulfur isotopic chain was obtained by multiplying the JLM isovector term by a factor of 2.0. The best fit λ_v and λ_w values are listed in Table III. Note that these values are now nearly constant and moreover close to 1.0. The remaining small variations of λ_v and λ_w are no longer significant considering the experimental errors. These results show the importance of correctly treating the isovector part of the JLM interaction for nuclei far from stability. A reasonable prescription for future calculations in this mass region would be to use the renormalized isovector JLM potential with λ_v and λ_w values of the order of 0.95.

The microscopic calculations can be compared in Fig. 9 with experimental elastic and inelastic angular distributions for several sulfur isotopes. Except for ^{36}S, a remarkable agreement is observed both in shape and magnitude. First, diffraction minima and maxima for elastic and inelastic scattering are very well reproduced. However, small discrepancies are observed at scattering angles larger than 60°. Note that the small overestimation of the charge rms radii discussed above does not seem to adversely affect either the position or the depth of the predicted diffraction minima. Similarly, the differences between phenomenological quadrupole deformations and those of the microscopic collective model are not evident from inspection of the calculated inelastic scattering differential cross sections shown in Fig. 9. Yet, the slight underestimation of the 2_1^+ cross-section noticeable in the case of ^{38}S may be hinting that its deformation should be larger. However, the observed difference between empirical and microscopic quadrupole deformations is probably overemphasized, since it is related to different methodologies and treatments of the scattering processes. In the case of ^{36}S, a renormalization of the transition densities entering the JLM calculation by a factor of 0.5 produces predictions which are in good agreement with experimental differential cross-

sections (dotted-dashed line in Fig. 9). This further confirms the fact that the microscopic collective model dramatically overestimates (by about a factor of 2) the deformation of the single closed shell nucleus ^{36}S. The good agreement between calculated and experimental angular distributions shows that the JLM interaction, folded with our microscopic densities, is a reliable tool for analyzing proton scattering off stable and unstable nuclei in the sulfur region away from the $N = 20$ shell closure.

A major goal in the study of neutron-rich nuclei is to find observables sensitive to the presence of neutron skins. As mentioned above, the microscopic collective model densities exhibit a neutron skin for the nuclei ^{38}S and ^{40}S. To investigate the influence of these unusual densities on the elastic and inelastic angular distributions, we have performed calculations similar to those described above where the neutron densities were taken to be equal to $\rho_n = \rho_p \times N/Z$, which excludes any neutron skin. Figure 10a) compares the resulting angular distributions (dashed line) with those calculated using the microscopic collective model densities (solid line). In both elastic and inelastic scattering the effects of the neutron skin show up more prominently at the larger scattering angles, where no data are presently available. Similar, but weaker effects are observed for ^{38}S, for which the neutron skin predicted by microscopic collective model calculations is less pronounced.

To assess the influence of a neutron skin at small scattering angles where data are available, the same calculations are shown on an expanded scale in Fig. 10b) together with the experimental data for ^{40}S. In the case of elastic scattering a slight shift of the first diffraction minimum is observed between the two calculations. The collective Hamiltonian calculation gives slightly better agreement with the data, but the poor statistics do not allow any definite conclusion to be drawn at present. The best hope to observe a neutron skin through proton scattering may be to obtain very precise elastic scattering data in the region of the first diffraction minimum where all the ingredients of the microscopic folding model calculations are fully under control.

VI. SUMMARY AND CONCLUSIONS

Elastic and inelastic cross sections for proton scattering on the unstable nucleus ^{40}S have been measured in inverse kinematics at 30 MeV. The use of a large array of strip detectors in coincidence with PPAC beam tracking detectors allowed us to obtain significant data despite a very low beam intensity (2000 pps) and a large incident beam emittance. This measurement extends the systematics of proton scattering on even-even sulfur isotopes from $N = 16$ and $N = 24$. Combination of these results with electromagnetic studies including Coulomb excitation measurements provides a unique data base to understand the evolution of the collective properties along the sulfur isotopic chain moving through the $N = 20$ shell closure towards the neutron rich side of the valley of stability.

The available proton scattering data on sulfur isotopes was first analyzed in the framework of a phenomenological optical model using the Becchetti-Greenlees parametrization and standard collective transition form factors. These calculations were in excellent agreement with the elastic scattering angular distributions over the whole isotopic chain. In the case of ^{40}S a β_2 value of 0.35 ± 0.05 is extracted for the 2_1^+ state found at an excitation energy of 860 ± 90 keV. This β_2 value is significantly larger than the β_2 deformation measured by Coulomb excitation, whereas both electromagnetic and (p,p') measurements yield similar deformation parameters for the stable sulfur isotopes . This difference was previously observed for ^{38}S. This behavior translates into M_n/M_p values which are larger than N/Z for the neutron rich isotopes in contrast to the values compatible with N/Z measured between $A = 32$ and 36. Overall the results indicate a strong neutron contribution to the excitation of the 2_1^+ states of ^{38}S and ^{40}S. A sudden change in the properties of the 2_1^+ state is observed between ^{36}S and ^{38}S due to the first two neutrons being in the $f_{7/2}$ orbital, while the additional two neutrons of ^{40}S seem to have little effect on these properties.

Microscopic coupled-channels calculations using microscopic collective model densities and a modified Jeukenne-Lejeune-Mahaux effective nucleon-nucleon interaction were also performed for sulfur isotopes. Through a suitable renormalization of the JLM isovector

term, a consistent representation of the elastic scattering data was obtained with values of the λ_v and λ_w renormalization parameters close to 1.0 and with little variation along the isotopic chain. The inelastic data are very well accounted for and the deformation parameters predicted by the microscopic collective model are near those extracted from the phenomenological analysis, with the exception of ^{36}S for which the microscopic collective model does not produce good predictions. The microscopic collective model densities exhibit a significant neutron skin for ^{38}S, which is even more pronounced in the case of ^{40}S, and the neutron transition densities are peaked at slightly larger radii than that for the protons. A comparison with calculations using neutron densities simply scaled from the proton densities by N/Z indicates that the neutron skin effects are greater at larger scattering angles but have a significant influence on the position of the first diffraction minimum. The angular range and statistics of the present elastic scattering data on the unstable sulfur isotopes do not allow a firm conclusion about the presence of a neutron skin to be established.

This work shows that the availability of data over a long isotopic chain is crucial to carry out a reliable microscopic analysis with consistent interaction parameters. The JLM interaction and the analysis procedure presented here will be a powerful tool in the future to test densities calculated by other theoretical calculations performed in the framework of the shell model [41], the quasi-particle random phase approximation, or the relativistic mean-field theory. The combination of Coulomb excitation and proton inelastic scattering is an attractive approach to assess the respective roles of protons and neutrons in deformations and excitations of nuclei. The availability of more extensive proton detection systems [42] and a new generation radioactive beam facility [43] will allow us to extend these studies further from stability and also to higher energies where the interaction potentials are better known.

We would like to warmly thank N. Alamanos, J.A. Carr, F.S. Dietrich and F. Petrovich for numerous valuable discussions. We are indebted to R. Alarcon and H.P. Blok for providing us with the ^{34}S and ^{36}S data in a tabulated form. This work was partly supported by the

National Science Foundation under contracts PHY-9528844, PHY-9602927, PHY-9523974 and PHY-9605207.

REFERENCES

* Present address Dept. of Physics, Florida State University, Tallahassee, FL 32306.

† Present address Cyclotron Institute, Texas A&M University, College Station, TX 77843.

‡ Present address Dept. of Physics, Millikin University, Decatur, IL 62522.

§ Present address Idaho National Engineering Laboratory, Idaho Falls, ID 83415.

¶ Present address TUNL, Duke University, Durham, NC 27708.

♯ Present address Dept. of Physics and Astronomy, Earlham College, Richmond, IN 47374.

♭ Present address Max Plank Insitut für Kernphysik, 69029 Heidelberg, Germany.

[1] T.R. Werner, J.A. Sheikh, W. Nazarewicz, M.R. Strayer, A.S. Umar, and M. Misu, Phys. Lett. **335B**, 259 (1994).

[2] T.R. Werner, J.A. Sheikh, M. Misu, W. Nazarewicz, J. Rikovska, K. Heeger, A.S. Umar, and M.R. Strayer, Nucl. Phys. **A597**, 327 (1996).

[3] J. Retamosa, E. Caurier, F. Nowacki, and A. Poves, Phys. Rev. C **55**, 1266 (1997).

[4] H. Scheit, T. Glasmacher, B.A. Brown, J.A. Brown, P.D. Cottle, P.G. Hansen, R. Harkewicz, M. Hellstrom, R.W. Ibbotson, J.K. Jewell, K.W. Kemper, D.J. Morrissey, M. Steiner, P. Thirolf, and M. Thoennessen, Phys. Rev. Lett. **77**, 3967 (1996).

[5] T. Glasmacher, B.A. Brown, M.J. Chromik, P.D. Cottle, M. Fauerbach, R.W. Ibbotson, K.W. Kemper, D.J. Morrissey, H. Scheit, D.W. Sklenicka, and M. Steiner, Phys. Lett. B **395B**, 163 (1997).

[6] F.D. Becchetti, Jr., and G.W. Greenlees, Phys. Rev. **182**, 1190 (1969).

[7] G. Kraus, P. Egelhof, C. Fischer, H. Geissel, A. Himmler, F. Nickel, G. Munzenberg, W. Schwab, A. Weiss, J. Friesse, A. Gillitzer, H.J. Korner, M. Peter, W.F. Henning, J.P. Schiffer, J.V. Kratz, L. Chulkov, M. Golovkov, A. Ogloblin, and B.A. Brown, Phys.

Rev. Lett **73**, 1773 (1994).

[8] A.A. Korsheninnikov, E.A. Kuzmin, E.Yu. Nikolsky, O.V. Bochkarev, S. Fukuda, S.A. Goncharov, S. Ito, T. Kobayashi, S. Momota, B.G. Novatsky, A.A. Ogloblin, A. Ozawa, V. Pribora, I. Tanihata, and K. Yoshida, Phys. Rev. Lett. **78**, 2317 (1997).

[9] J.K. Jewell, L.A. Riley, P.D. Cottle, K.W. Kemper, T. Glasmacher, R.W. Ibbotson, H. Scheit, M. Chromik, Y. Blumenfeld, S.E. Hirzebruch, F. Maréchal, and T. Suomijärvi, submitted to Phys. Lett. B.

[10] J.H. Kelley, T. Suomijärvi, S.E. Hirzebruch, A. Azhari, D. Bazin, Y. Blumenfeld, J.A. Brown, P.D. Cottle, S. Danczyk, M. Fauerbach, T. Glasmacher, J.K¿ Jewell, K.W. Kemper, F. Maréchal, D.J. Morrissey, S. Ottini, J.A. Scarpaci, and P. Thirolf, Phys. Rev. C **56**, R1206 (1997).

[11] T. Suomijärvi, J.H. Kelley, S.E. Hirzebruch, A. Azhari, D. Bazin, Y. Blumenfeld, J.A. Brown, P.D. Cottle, S. Danczik, M. Fauerbach, T. Glasmacher, J.K. Jewell, K.W. Kemper, F. Maréchal, D.J. Morrissey, S. Ottini, J.A. Scarpaci, and P. Thirolf, Nucl. Phys. **A616**, 295c (1997).

[12] R. de Leo, G. D'Erasmo, E.M. Fiore, G. Guarino, and A. Pantaleo, Nuovo Cimento **59A**, 101 (1980).

[13] R. Alarcon, J. Rapaport, R.T. Kovzes, W.H. Moore, and B.A. Brown, Phys. Rev. C **31**, 697 (1985).

[14] A. Hogenbirk, H.P. Blok, M.G.E. Brand, A.G.M. van Hees, J.F.A. van Hienen, and F.A. Jansen, Nucl. Phys. **A516**, 205 (1990).

[15] B.M. Sherrill, D.J. Morrissey, J.A. Nolen, Jr., N. Orr, and J.A. Winger, Nucl. Instrum. Methods Phys. Res. **B70**, 298 (1992).

[16] F. Maréchal, PhD Thesis, Université d'Orsay (1998), Internal Report IPNO-T-98-02.

[17] D. Swan, J. Yurkon, and D. Morrissey, Nucl. Instrum. Methods Phys. Res. **A348**, 314 (1994).

[18] J. Raynal, Phys. Rev. C **23**, 2571 (1981). J. Raynal, CEA report No CEA-N-2772, 1994.

[19] A.M. Bernstein, V.R. Brown, and V.A. Madsen, Phys. Lett. **103B**, 255 (1981).

[20] A.M. Bernstein, V.R. Brown, and V.A. Madsen, Comments Nucl. Part. Phys. **11**, 203 (1983).

[21] M.A. Kennedy, P.D. Cottle and K.W. Kemper, Phys. Rev. C **46**, 1811 (1992).

[22] S. Raman, C.H. Malarkey, W.T. Milner, C.W. Nestor, Jr., and P.H. Stelson, Atomic Data and Nuclear Data Tables **36**, 1 (1987).

[23] E. Bauge, J.P. Delaroche, and M. Girod, Phys. Rev. C **58**, 1118 (1998).

[24] R.K. Sandor, H.P. Blok, M. Girod, M.N. Harakeh, C.W. de Jager, and H. De Vries, Nucl. Phys. **A 551**, 349 (1993).

[25] J.F. Berger, M. Girod, and D. Gogny, Comp. Phys. Comm., **63**, 365 (1990); J. Dechargé, and D. Gogny, Phys. Rev. C **21**, 1568 (1980).

[26] J.P. Jeukenne, A. Lejeune, and C. Mahaux, Phys. Rev. C **10**, 1391 (1974).

[27] J.P. Jeukenne, A. Lejeune, and C. Mahaux, Phys. Rep. **25C**, 83 (1976).

[28] J.P. Jeukenne, A. Lejeune, and C. Mahaux, Phys. Rev. C **15**, 10 (1977).

[29] J.P. Jeukenne, A. Lejeune, and C. Mahaux, Phys. Rev. C **16**, 80 (1977).

[30] J.W. Negele and K. Yazaki, Phys. Rev. Lett. **47**, 71 (1981).

[31] M. Pignanelli, A.Micheletti, R. De Leo, S. Brandenburg, and M.N. Harakeh, Phys. Rev. C **33**, 40 (1986).

[32] T.Cheon, K. Takayanagi, and K. Yazaki, Nucl. Phys. **A437**, 301 (1985).

[33] R.R. Scheerbaum, Nucl. Phys. **A257**, 77 (1976).

[34] H. Sherif and S. Blair, Phys. Lett. **26B**, 489 (1968).

[35] D. Rychel, H.J. Emrich, H. Miska, R. Gyufko, and C.A. Wiedner, Phys. Lett. **130B**, 5 (1983).

[36] G.C. Li, M.R. Yearian, and I. Sick, Phys. Rev. C **9**, 1861 (1974).

[37] J.J. Kelly, M.A. Khandaker, P. Boberg, A.E. Feldman, B.S. Flanders, S. Hyman, H. Seifert, P. Karen, B.E. Norum, P. Welch, S. Nanda, and A. Saha, Phys. Rev. C **44**, 1963 (1991).

[38] U. Wörsdörfer, H.J. Emrich, H. Miska, D. Rychel, R. Gyufko, and C.A. Weidner, Nucl. Phys. **A438**, 711 (1985).

[39] F.S. Dietrich and F. Petrovich, AIP conference proceedings **124** (1985) J. Rapaport, R.W. Finlay, S.M. Grimes, and F.S. Dietrich edts, page 90.

[40] M.D. Cortina-Gil, A. Pakou, N. Alamanos, W. Mittig, P. Roussel-Chomaz, F. Auger, J. Barette, Y. Blumenfeld, J.M. Casandjian, M. Chartier, F. Dietrich, V. Fekou-Youmbi, B. Fernandez, N. Frascaria, A. Gillibert, H. Laurent, A. Lepine-Szily, N. Orr, V. Pascalon, J.A. Scarpaci, J.L. Sida, and T. Suomijärvi, Nucl. Phys. **A641**, 263 (1998).

[41] N. Alamanos, F. Auger, B.A. Brown, and A. Pakou, J. Phys. G. **24**, 1541 (1998).

[42] Y. Blumenfeld, F. Auger, J.E. Sauvestre, F. Maréchal, S. Ottini, N. Alamanos, A. Barbier, D. Beaumel, B. Bonnereau, D. Charlet, J.F. Clavelin, P. Courtat, P. Delbourgo-Salvador, R. Douet, M. Engrand, T. Ethvignot, A. Gillibert, E. Khan, V. Lapoux, A. Lagoyannis, L. Lavergne, S. Lebon, P. Lelong, A. Lesage, V. Le Ven, I. Lhenry, J.M. Martin, A. Musumarra, S. Pita, L. Petizon, J. Pouthas, A. Richard, D. Rougier, D. Santonocito, J.A. Scarpaci, J.L. Sida, C. Soulet, J.S. Stutzmann, T. Suomijärvi, M. Szmigiel, P. Volkov, and G. Voltolini, Nucl. Instrum. Methods Phys. Res. **A421**, 471

(1999).

[43] The K500×K1200: A Coupled Cyclotron Facility at the NSCL/MSU, NSCL Report MSUCL-939 (1994).

FIGURES

FIG. 1. Schematic diagram of the experimental setup. Four silicon-strip telescopes that detected recoiling protons from a CH_2 target were placed on each side of the beam direction. A plastic phoswich detector was placed at 0° and measured both incident beam and scattered fragments. Two PPACs placed before the target were used to track the beam event by event.

FIG. 2. Calculated energy-angle correlations in the laboratory frame for recoiling protons for elastic scattering (solid curve) and inelastic scattering to the 2_1^+ state located at 860 keV (dashed curve) in ^{40}S. The vertical dashed lines indicate the angular ranges covered by the different telescopes.

FIG. 3. Energy vs. angle scatterplot measured for recoiling protons in coincidence with ^{40}S ejectiles (a). Calculated kinematic lines for the ground state (solid curve), the 2_1^+ state at 860 keV and a hypothetical state at 2.9 MeV (dashed curves) are shown. (b) Same as (a) for ^{38}S (from Ref. [10]).

FIG. 4. Excitation energy spectrum for ^{40}S scattering on protons at 30 MeV/nucleon integrated over the total *cm* angular range $20° \leq \Theta_{cm} \leq 46°$ (a) and over the 28°-36° angular bin (b). The dashed lines are gaussian fits to the elastic and inelastic peaks. The solid line is the sum of the two contributions.

FIG. 5. Angular distributions for the ground state (open circles) and the first excited state (filled circles) in the ^{40}S(p,p') reaction at 30 MeV/nucleon. DWBA calculations using the Becchetti-Greenlees optical potential are shown for the ground state (solid line) and for the 2^+ state (dashed line) (see text).

FIG. 6. Angular distributions for the ground state (open circles) and the 2_1^+ state (filled circles) in the ^{32}S(p,p') reaction at 29.6 MeV, the ^{34}S(p,p') reaction at 29.8 MeV, the ^{36}S(p,p') reaction at 28.0 MeV, the ^{38}S(p,p') reaction at 39.0 MeV/nucleon and in the ^{40}S(p,p') reaction at 30.0 MeV/nucleon. The experimental data are from Refs. [12–14,10] and the present work, respectively. DWBA calculations using the Becchetti-Greenlees optical potential and a standard collective form factor are shown for the ground state (solid line) and the 2_1^+ state (dashed line) (see text).

FIG. 7. Microscopic collective model predictions for the ground state and transition densities to the 2_1^+ state for even-even sulfur isotopes ranging from ^{32}S to ^{40}S. The solid lines are for the proton densities whereas the dashed lines are for the neutron densities.

FIG. 8. Comparison between experimental (solid line) and predicted (dashed line), monopole (upper panels) and $0_{gs}^+ \rightarrow 2_1^+$ transition (lower panels) charge densities for ^{32}S, ^{34}S, and ^{36}S. Experimental data is extracted from [35,37,38]. Charge densities are obtained by convoluting the calculated proton densities with the proton charge smearing form factor.

FIG. 9. Data are the same as in Fig. 6. Microscopic coupled channel calculations using microscopic collective model densities and the JLM nucleon-nucleon interaction for the ground state (solid line) and the 2_1^+ state (dashed line) (see text). For ^{36}S, the dotted-dashed line corresponds to calculations with renormalized transition densities as described in the text.

FIG. 10. (a) Solid line: same calculation as in Fig. 9 for ^{40}S. Dashed line: microscopic coupled channel calculations using microscopic collective model proton densities and neutron densities scaled by N/Z from the proton densities. (b) Same calculations shown in comparison with the ^{40}S data using an expanded scale.

TABLES

TABLE I. Compilation of the properties of the ground and 2_1^+ states in sulfur isotopes. Energies and β_2^{em} values are from Ref. [22] ($^{32-36}$S) and Ref. [4] (^{38,40}S). $\beta_2^{pp'}$ values are from Refs. [12] (^{32}S), [13] (^{34}S), [14] (^{36}S), [10] (^{38}S) and from this work (^{40}S). $\beta_2^{pp'}$ (BG) are from our reanalysis of the data of Refs. [12–14] using the Becchetti-Greenlees optical potential. M_n/M_p ratios were calculated using Eq. (1) and $\beta_2^{pp'}$ (BG) values. The rms charge radii r_{rms}^c for $^{32-36}$S are from Ref. [35].

	E_{2+}^* (MeV)	r_{rms}^c (fm)	β_2^{em}	$\beta_2^{pp'}$	$\beta_2^{pp'}(BG)$	$(M_n/M_p)/(N/Z)$
^{32}S	2.23	3.248	0.31±0.01	0.28±0.02	0.28±0.02	0.84±0.17
^{34}S	2.12	3.281	0.25±0.01	0.28±0.01	0.24±0.02	0.91±0.11
^{36}S	3.29	3.278	0.16±0.02	0.18	0.18±0.02	1.13±0.27
^{38}S	1.29		0.25±0.02	0.35±0.04	0.35±0.04	1.50±0.30
^{40}S	0.89		0.28±0.02	0.35±0.05	0.35±0.05	1.25±0.25

TABLE II. Energies of the 2_1^+ state, rms charge radii, matter, proton and neutron deformations and M_n/M_p ratios from the microscopic collective model calculations described in the text.

	E_{2+}^* (MeV)	r_{rms}^c (fm)	β_2^m	β_2^p	β_2^n	$(M_n/M_p)/(N/Z)$
^{32}S	1.996	3.324	0.311	0.317	0.306	0.965
^{34}S	2.343	3.327	0.268	0.280	0.258	0.921
^{36}S	2.408	3.353	0.290	0.283	0.296	1.043
^{38}S	2.166	3.372	0.286	0.272	0.296	1.085
^{40}S	1.713	3.398	0.303	0.283	0.317	1.120

TABLE III. Potential depth normalization factors for the real and imaginary parts of the central (λ_v, λ_w) potential. These values give the best fit to the proton scattering data.

	λ_v	λ_w
^{32}S	0.95	0.95
^{34}S	0.93	0.98
^{36}S	0.95	0.93
^{38}S	0.95	0.92
^{40}S	0.94	0.93

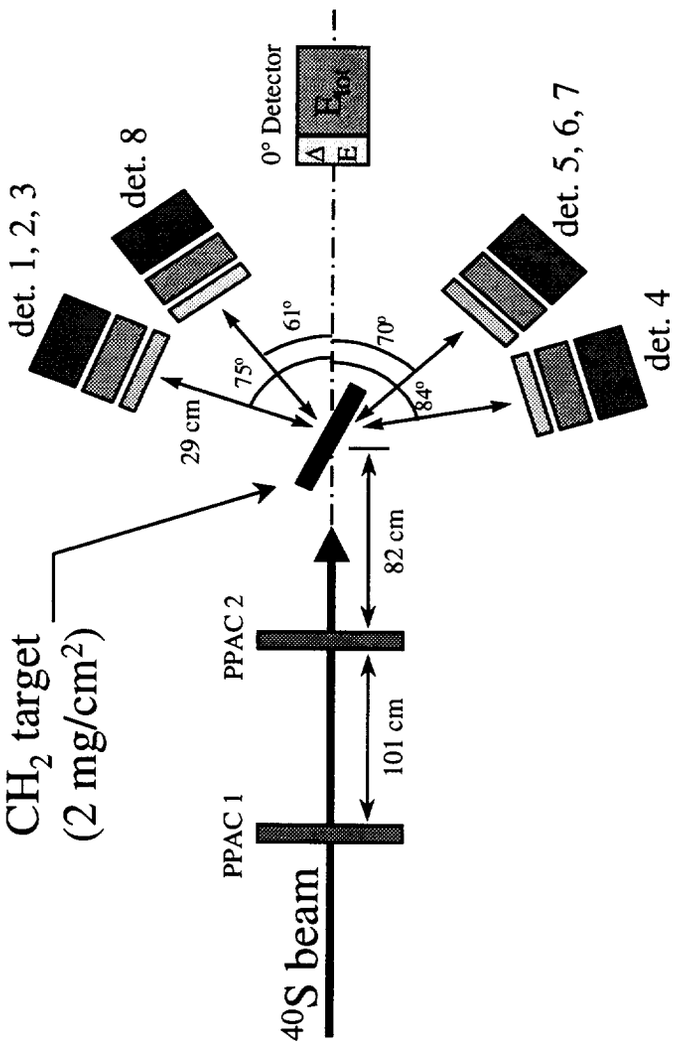
^{40}S beam
PPAC 1
PPAC 2
101 cm
82 cm
CH_2 target
(2 mg/cm^2)
29 cm
75°
61°
70°
84°
det. 1, 2, 3
det. 8
0° Detector
E_{tot}
ΔE
det. 5, 6, 7
det. 4

Fig. 1

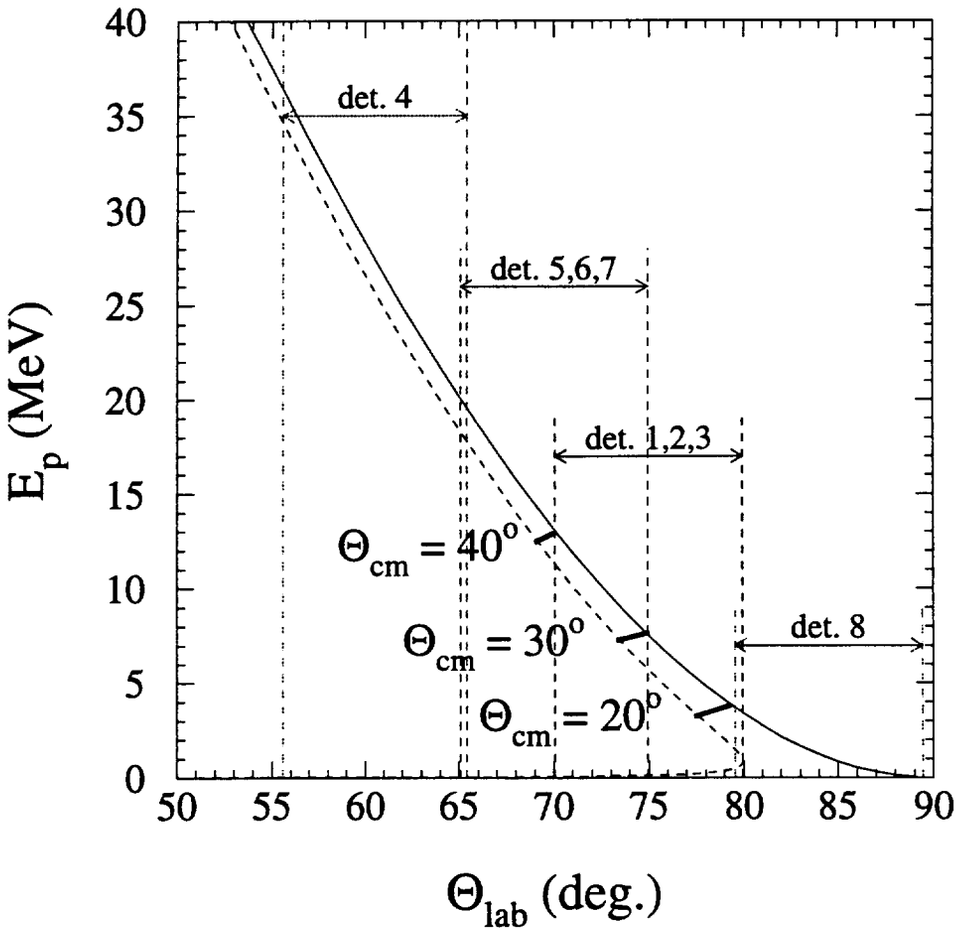
40
35
30
25
20
15
10
5
0
50
55
60
65
70
75
80
85
90
E_p (MeV)
Θ_{lab} (deg.)
det. 4
det. 5,6,7
det. 1,2,3
det. 8
$\Theta_{cm} = 40^o$
$\Theta_{cm} = 30^o$
$\Theta_{cm} = 20^o$

Fig. 2

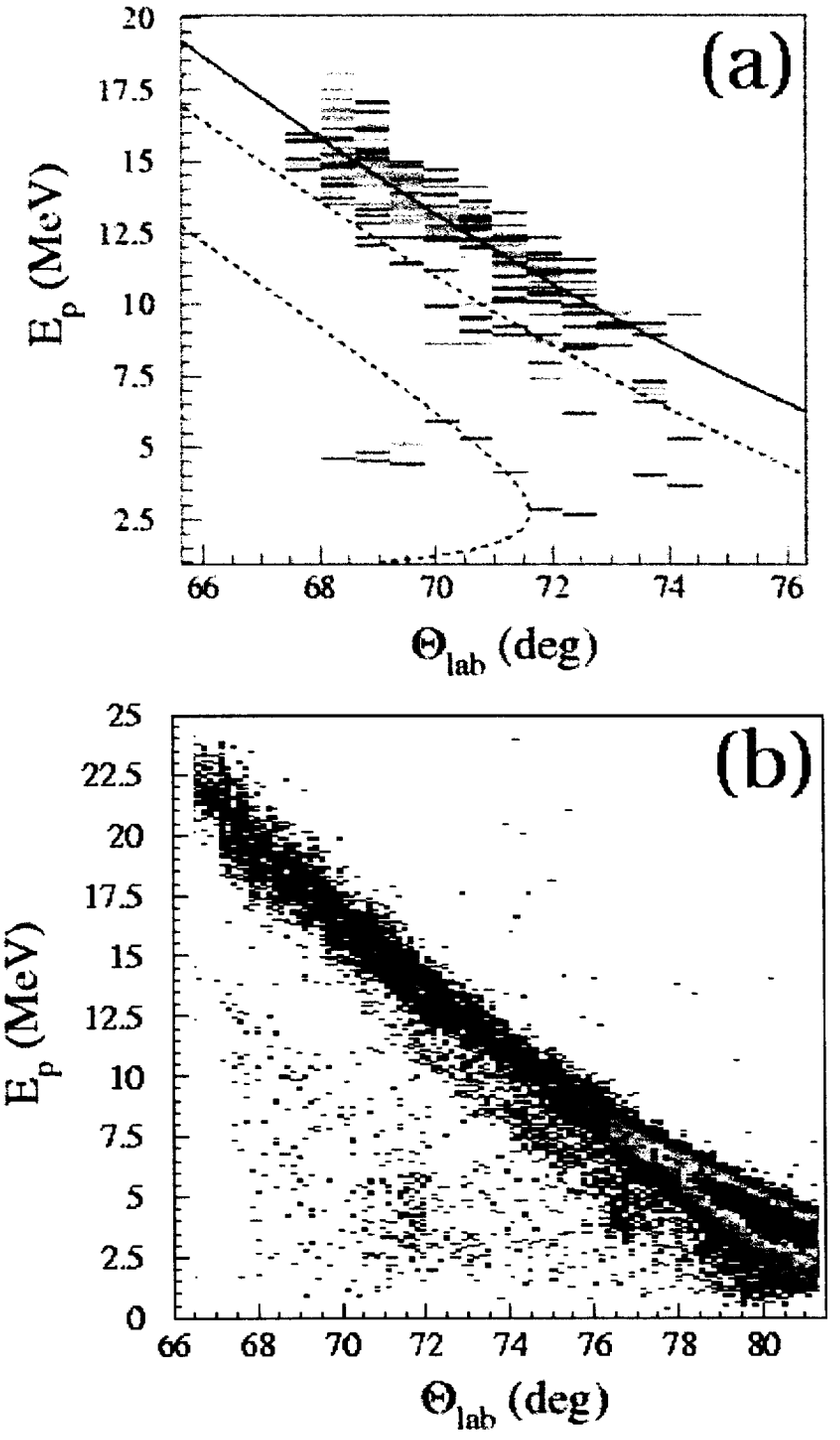

Fig. 3

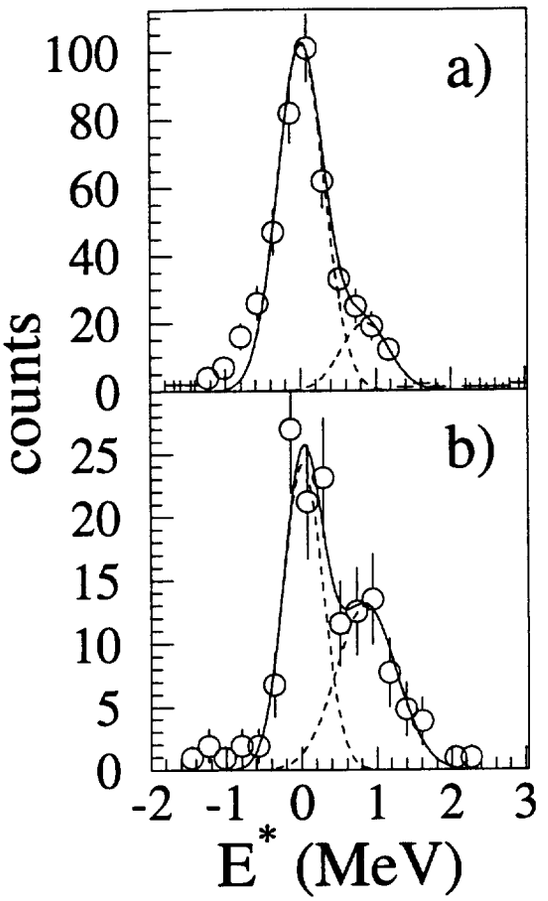
a)
b)
counts
100
80
60
40
20
0
25
20
15
10
5
0
-2
-1
0
1
2
3
E* (MeV)

Fig. 4

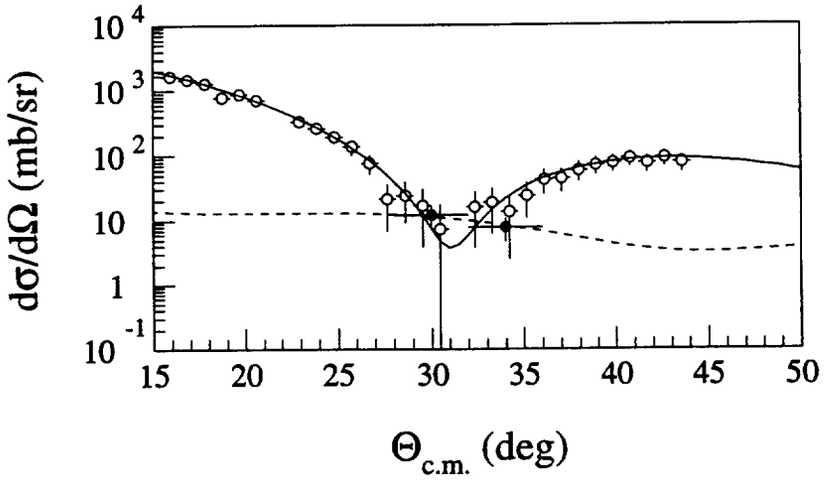
dσ/dΩ (mb/sr)
10 4
10 3
10 2
10
1
10 -1
15
20
25
30
35
40
45
50
Θc.m. (deg)

Fig. 5

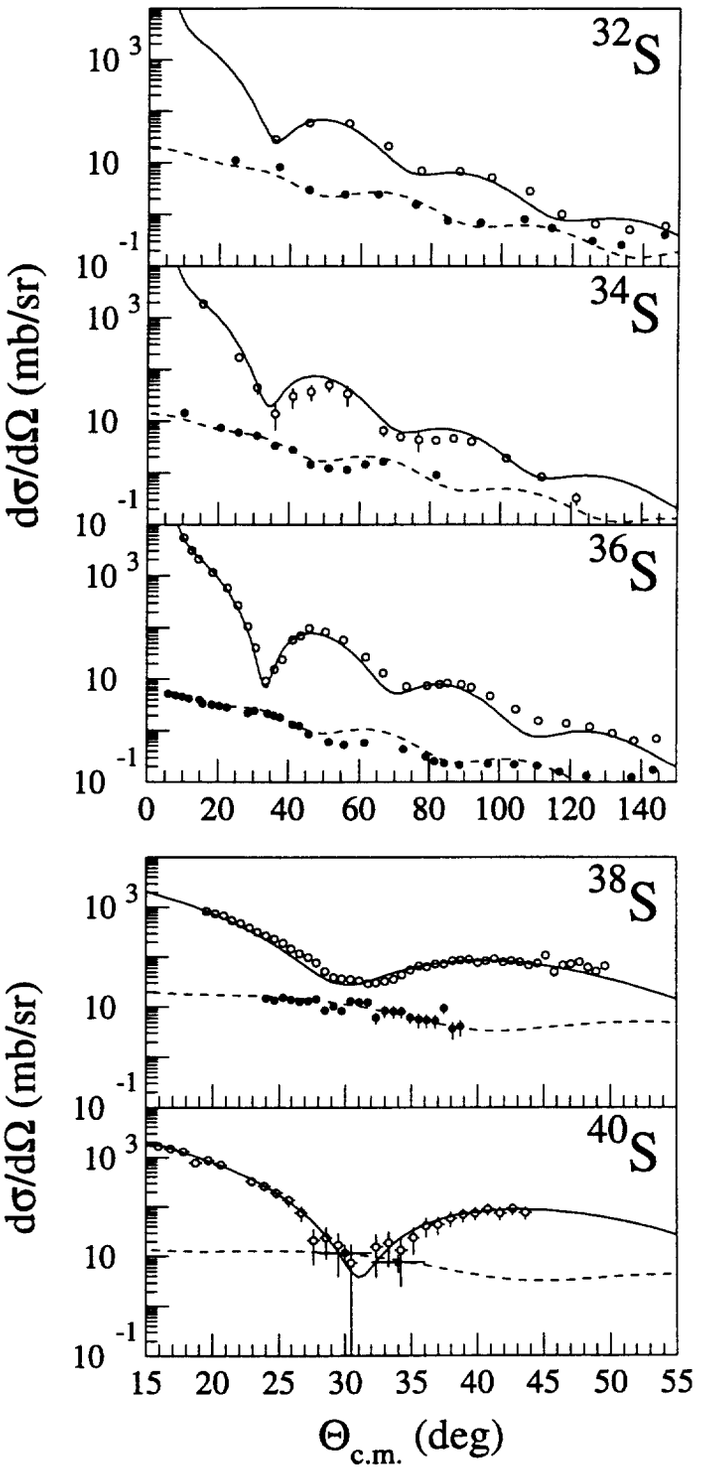
^{32}S
^{34}S
^{36}S
^{38}S
^{40}S
dσ/dΩ (mb/sr)
dσ/dΩ (mb/sr)
10^3
10
10^{-1}
0 20 40 60 80 100 120 140
15 20 25 30 35 40 45 50 55
$\Theta_{c.m.}$ (deg)

Fig. 6

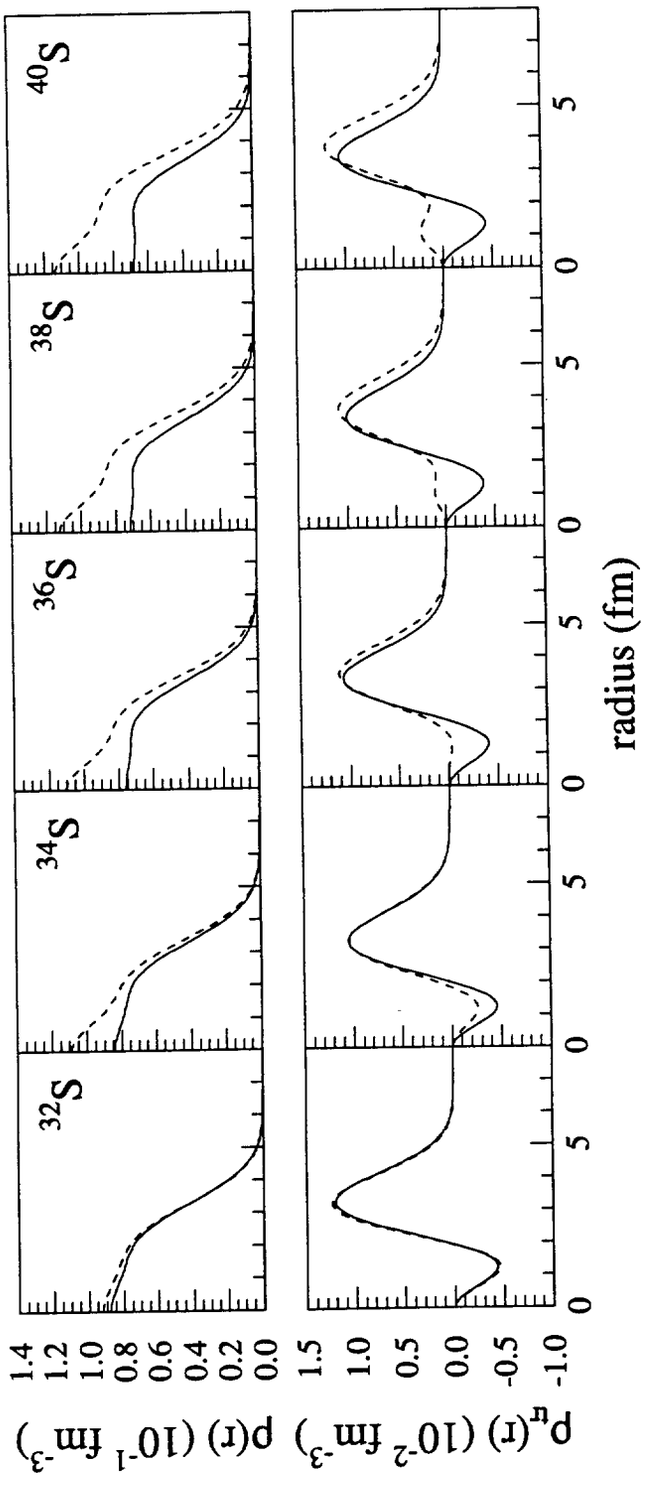
^{32}S
^{34}S
^{36}S
^{38}S
^{40}S
1.4
1.2
1.0
0.8
0.6
0.4
0.2
0.0
1.5
1.0
0.5
0.0
-0.5
-1.0
0
5
0
5
0
5
0
5
radius (fm)
$\rho_n(r)$ (10^{-2} fm^{-3}) $\rho(r)$ (10^{-1} fm^{-3})

Fig. 7

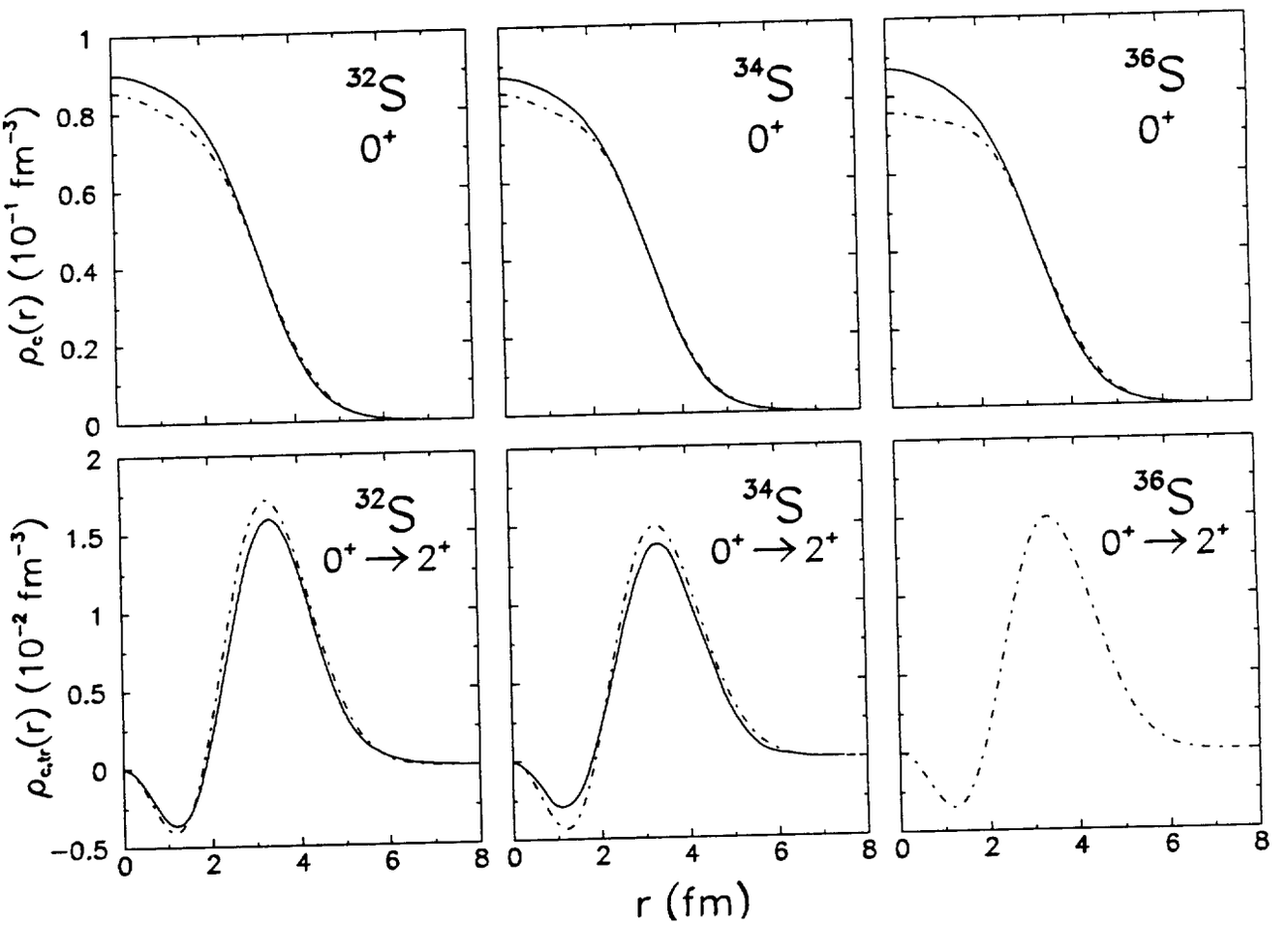
^{32}S
0^+
^{34}S
0^+
^{36}S
0^+
^{32}S
$0^+ \rightarrow 2^+$
^{34}S
$0^+ \rightarrow 2^+$
^{36}S
$0^+ \rightarrow 2^+$
$\rho_c(r)$ (10^{-1} fm^{-3})
$\rho_{c,tr}(r)$ (10^{-2} fm^{-3})
r (fm)

Fig. 8

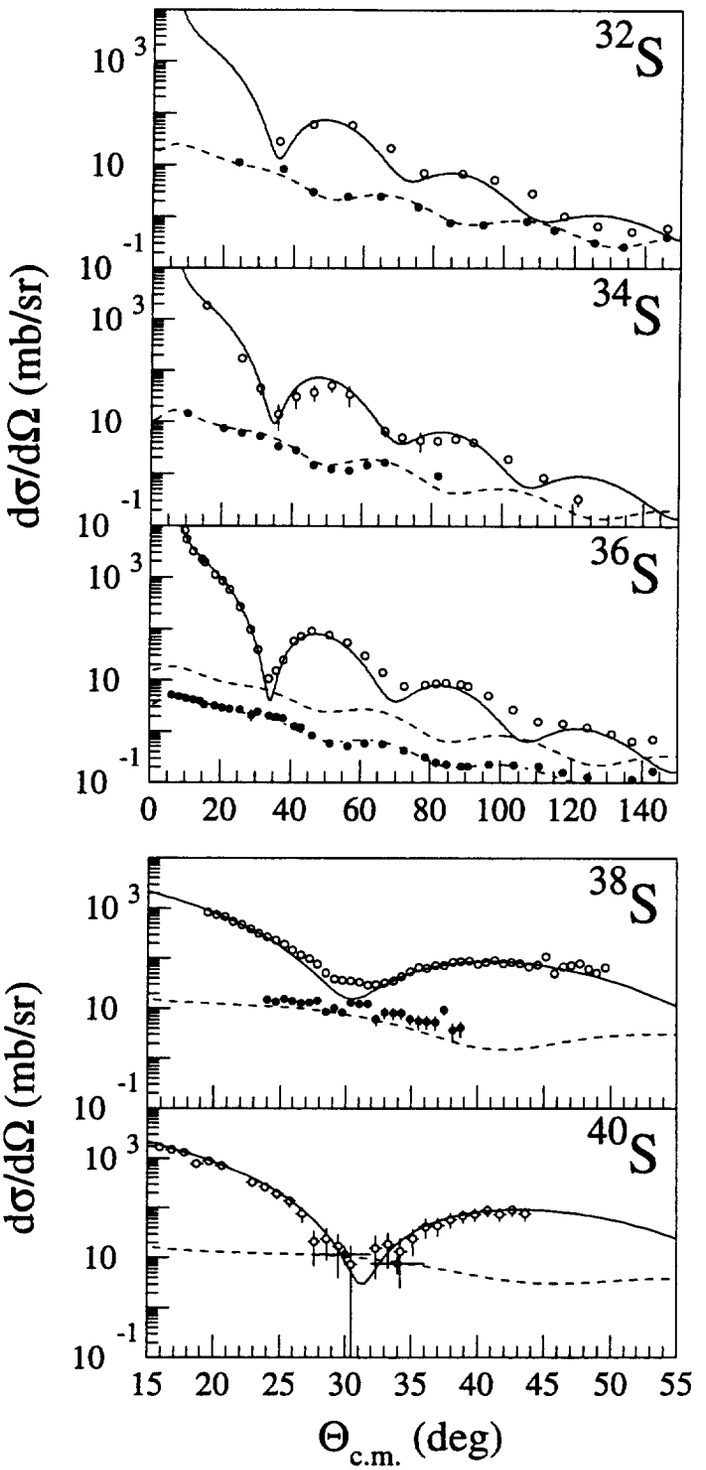

Fig. 9

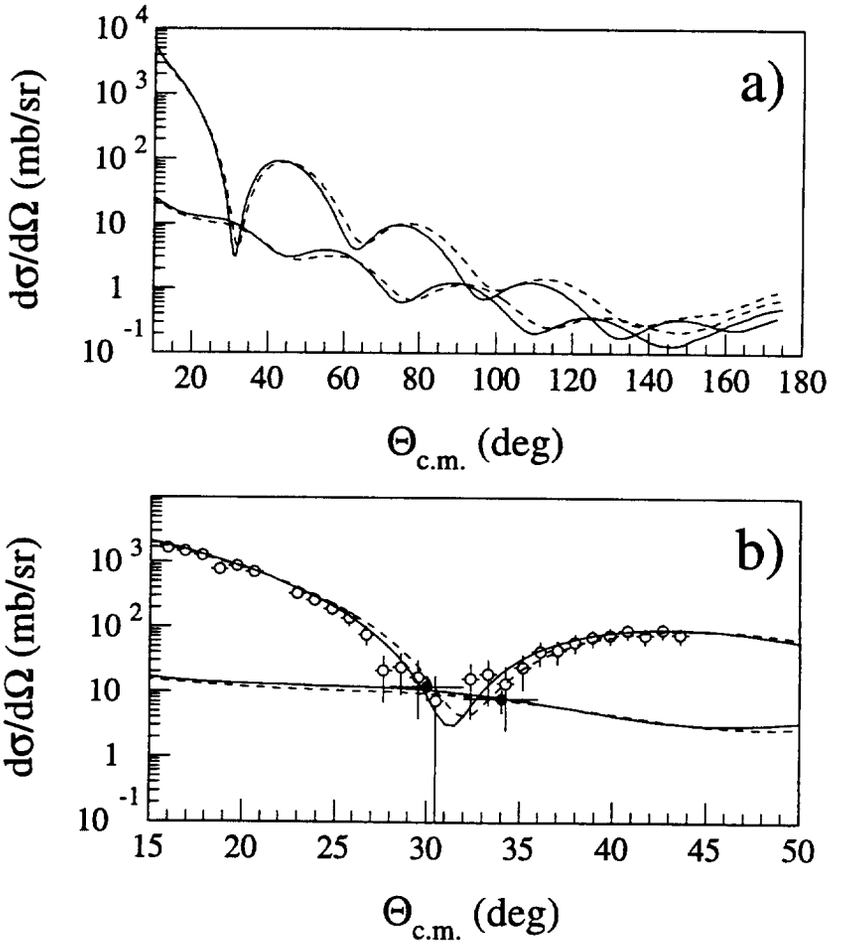
a)
b)
dσ/dΩ (mb/sr)
Θc.m. (deg)
10 4
10 3
10 2
10
1
10 -1
20 40 60 80 100 120 140 160 180
15 20 25 30 35 40 45 50

Fig. 10